Multiscale CO budget estimates across South America: quantifying local sources and long range transport

Pablo Lichtig[1,2], Benjamin Gaubert[3], Louisa K. Emmons[3], Duseong S. Jo[3], Patrick Callaghan[3], Sergio Ibarra-Espinosa[4], Laura Dawidowski[1], Guy P. Brasseur[5], Gabriele Pfister[3]

[1]National Comission of Atomic Energy, Buenos Aires, Argentina
[2]National Counsel of Science and Technology, Buenos Aires, Argentina
[3]National Center for Atmospheric Research, Boulder, Co, USA
[4]National Oceanographic and Atmospheric Administration, Boulder, CO, USA
[5]Max Planck Institute for Meteorology, Hamburg, Germany

Key Points:

- We employ the Multi-Scale infrastructure for Chemistry and Aerosols to quantify the budget of CO in South America during 2019.
- Most of the variability in the CO burden is explained by the variability in biomass burning emissions.
- Biomass burning in Central Africa is a relevant contributor to CO in all of the continent, including the southern region.

Corresponding author: Guy Brasseur, guy.brasseur@mpimet.mpg.de

Corresponding author: Pablo Lichtig, pablolichtig@cnea.gov.ar

Abstract

South America is a large continent situated mostly in the Southern Hemisphere (SH) with complex topography and diverse emissions sources. However, the atmospheric chemistry of this region has been historically understudied. Here, we employ the Multi-Scale Infrastructure for Chemistry and Aerosols, a novel global circulation model with regional refinement capabilities and full chemistry, to explore the sources and distribution of the carbon monoxide (CO) tropospheric column in South America during 2019, and also to assess the effect that South American primary emissions have over the rest of the world. Most of the CO over South America can be explained either by NMVOC secondary chemical production or by biomass burning emissions, with biomass burning as the main explanation for the variability in CO. Biomass burning in Central Africa is a relevant contributor to CO in all of the continent, including the southern tip. Biogenic emissions play a dual role in CO concentrations: they provide volatile organic compounds that contribute to the secondary CO production, but they also destroy OH, which limits the chemical production and destruction of CO. As a net effect, the lifetime of CO is extended to ∼120 days on average over the Amazon, while still being in the range of 30–60 days in the rest of South America.

Plain Language Summary

We use the Multi-Scale Infrastructure for Chemistry and Aerosols, a global model with regional refinement, to study the origins of carbon monoxide (CO) in South America during 2019. The main sources of CO are the secondary production from non-volatile organic compounds and the biomass burning primary emissions. The main source of temporal variability in the whole are the biomass burning emissions. We show that biomass burning in central Africa is a relevant source of South American CO during all year in all of the continent, including the furthermost south.

1 Introduction

Carbon monoxide (CO) is an atmospheric trace gas constituent that plays an important role in tropospheric chemistry (Levy, 1971; Gaubert et al., 2017). Globally, the CO primary sources result from incomplete combustion of fossil fuel from industrial, road transportation and residential sectors, and from biomass burning, including for cooking, heating and wildfires (Duncan et al., 2007). Other minor sources include biological processes, mainly by land's vegetation, with minor contributions from oceanic emissions. The CO oxidation into CO_2 (Eq. 1) plays an essential role in atmospheric chemistry as a major sink of hydroxyl radical (OH), and a source of hydroperoxyl radical (HO_2) (Stone et al., 2012). CO has a relatively long lifetime (weeks to months), and is mostly emitted by anthropogenic emissions or biomass burning (Gaubert et al., 2016). Hence, it is often used as a tracer for pollution sources and transport, and will be the main focus of this study (Edwards, 2004).

$$\mathrm{CO} + \mathrm{OH} \xrightarrow{\mathrm{O_2}} \mathrm{CO_2} + \mathrm{HO_2} \tag{1}$$

Around 50% of CO is formed in the atmosphere as a result of the oxidation of methane (CH_4) and non-methane volatile organic compounds (NMVOCs) (Duncan et al., 2007; Stein et al., 2014; Gaubert et al., 2016), either through photolysis or through multiple oxidation process. Aside from photolysis, most organic compounds including CH_4 and NMVOCs are oxidized mainly or exclusively by OH (Seinfeld & Pandis, 2016), as shown in Eq. 2. The oxidation process by OH produces organic peroxy radicals (RO_2), which can later produce CO through multiple reaction pathways.

$$\mathrm{RH(CH_4, NMVOC)} + \mathrm{OH} \xrightarrow{\mathrm{O_2}} \mathrm{RO_2} + \mathrm{H_2O} \longrightarrow \alpha CO \tag{2}$$

The yield α varies according to oxidation pathways, including the NO_x levels, and products generated (Pfister et al., 2008; Grant et al., 2010). Therefore, the net effect of a change in OH on the CO budget is not always straightforward, as OH acts both as a source and a sink for CO (Gaubert et al., 2016, 2017).

CO has been studied extensively in the Northern Hemisphere where even the background levels are almost twice as large as in the Southern Hemisphere (Novelli, 2003). Comparisons with the satellite CO observations indicate that global models have remaining difficulties to simulate CO during the winter and spring with a strong underestimation in the Northern Hemisphere extratropics (Shindell et al., 2006), mostly because of underestimation in emissions (Stein et al., 2014; Gaubert et al., 2020) and representation of the chemistry (Naik et al., 2013; Müller et al., 2018; Gaubert et al., 2023). High CO amounts from biomass burning were first observed in the 1990's from the Measurement of Air Pollution from Satellites (MAPS) experiment (Watson et al., 1990). Biomass burning emissions are the main driver of CO levels in the tropics and in the Southern Hemisphere, explaining the inter-model differences in modeled CO levels, with a strong interannual variability(Edwards, 2004; Shindell et al., 2006).

As reported by Paton-Walsh et al. (2022), the Southern Hemisphere, in contrast, remains largely understudied. It holds only $\sim$ 10% of the global population, and is $\sim$80% ocean. It also holds the cleanest atmospheric conditions, found in the Southern Ocean. South America is a continent extending from 55.8 °S - 12.5 °N and 81.4 °W - 34.3 °W. It has a large variety of vegetation, soil and climate regions (de Miranda et al., 2022), ranging from the rainforests in the Amazon Basin to the desert in Atacama, the plains in the Pampas, the Patagonian Steppe and the continental ice of southern Chile.

The goal of this study is to quantify the local and long range origins of CO in South America. We utilize the newly developed Multi-Scale Infrastructure for Chemistry and Aerosols version 0 (MUSICAv0) (Pfister et al., 2020; Schwantes et al., 2022) with regional mesh refinement over South America. This study is the first that applies MUSICA over South America. We employ a system of CO tagged tracers to quantify the CO budget and to identify geographical origins of CO by sources.

In section 2, we first describe the general model setup (subsec. 2.1) and a CO tagged tracer mechanism (subsec. 2.2). We then describe the evaluation of the model results using satellite data (subsec. 2.3) and the methodology to evaluate CO sources and CO variability using the tags (subsec. 2.4). In section 3, we start by evaluating the model with satellite CO data (subsec. 3.1). We then evaluate the CO budget both globally and over South America, and compare the results of the MUSICAv0 refined simulation with a standard, control run with a global coarse grid (subsec. 3.2). In section 3.3, we analyze the effect on the burden and the variability, as well as the spatial distribution of the CO chemical lifetime. We further discuss the variability and geographical origin of CO in 3.3.2. In section 3.3.3, we analyze the effect that South American primary emissions are having in the CO burden over the rest of the world. Finally, we summarize our results and conclusions in section 4, and close the paper discussing future perspectives.

2 Methods

2.1 Model description and setup

We use MUSICAv0, which is part of the Community Earth System Model (Danabasoglu et al., 2020) version 2.2 (CESM2.2), an open source Earth System Model maintained by the National Center for Atmospheric Research (NCAR). MUSICAv0 is a configuration of the Community Atmosphere Model with Chemistry (CAM-chem) (Emmons et al., 2020; Tilmes et al., 2019) with a spectral element (SE) dynamical core that allows for regional refinement (Lauritzen et al., 2018; Schwantes et al., 2022; Tang et al., 2022, 2023). The model is run coupled to the Community Land Model (CLM) v5.0 (Lawrence et al., 2019)

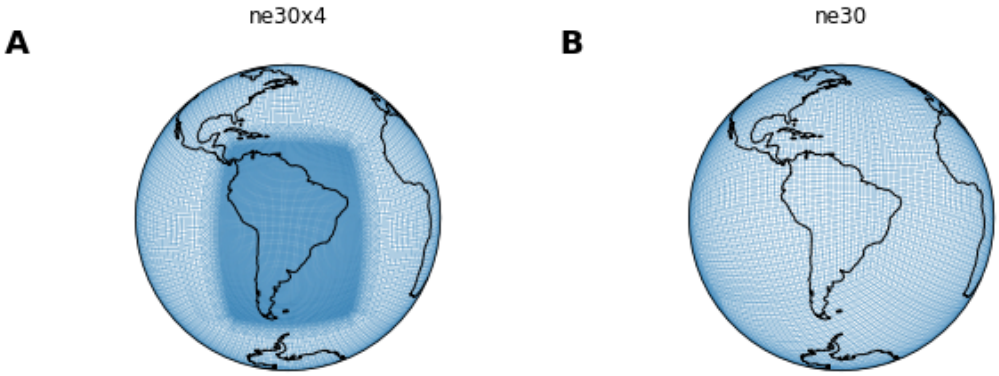

Figure 1. Model meshes

to interactively simulate land processes, the deposition of gases and aerosols and biogenic emissions. The latter are estimated from the Model of Emissions of Gases and Aerosols from Nature (MEGAN) version 2.1 (Guenther et al., 2012) and depend interactively on the modeled temperature, solar radiation, leaf area index (LAI) and other modeled parameters. We employ prescribed monthly LAI at 0.25° resolution, denoted as satellite phenology. The effect resulting from this configuration is discussed in detail in Jo et al. (2023). In this paper, we perform a global simulation including a mesh refinement over South America (ne30x4, [∼28 km]) and a control simulation at uniform resolution (ne30, [∼111 km]), as shown in Fig. 1. Unless otherwise stated for specific parameters, the two simulations should be assumed to have the same setup. The ne30 simulation is run with a physical time step of 1800 s, while the ne30x4 simulation uses a time step of 450 s. Both simulations have 32 vertical layers, with ∼7 model layers below the planetary boundary layer height (PBLH) and ∼15 layers below the stratosphere, and a hybrid terrain following vertical coordinate. The Cloud Layers Unified by Binormals (CLUBB) scheme is used for shallow convection, cloud macrophysics and boundary layer turbulence (Bogenschutz et al., 2013), and the MG2 scheme is used for cloud microphysics (Gettelman & Morrison, 2015). The ZM scheme (Zhang & McFarlane, 1995) is used for deep convection. We nudge relevant meteorological parameters (T, U, V) to the Modern-Era Retrospective Analysis for Research and Applications, Version 2, (MERRA-2) (Gelaro et al., 2017), with a 12 h relaxation time.

As a chemical mechanism, we employ the Model for Ozone and Related Chemical Tracers with tropospheric and stratospheric chemistry (MOZART-TS1) (Emmons et al., 2020) and the Modal Aerosol Model with 4 modes (MAM4) (Liu et al., 2016). We use anthropogenic emissions from the CAMS-GLOB-ANT version 5.3, and aircraft emissions from CAMS-GLOB-AIR version 2.1 (Soulie et al., 2023). The daily fire emissions are prescribed from the Fire Inventory from NCAR version 2.5 (FINN2.5), using both MODIS and VIIRS fire detection (Wiedinmyer et al., 2023). The chemistry mechanism also includes a volatility basis set representation of secondary organic aerosol (Tilmes et al., 2019) with NO_x[1] dependent pathways for secondary organic aerosol (SOA) formation (Jo et al., 2021). We include the update of the HO_2 heterogeneous uptake introduced by Gaubert et al. (2020).

The spin-up simulations for the land model and the atmospheric model are performed separately. The land model is spun-up for a year at the final resolution, with a

[1] NO_x is the sum of nitrogen monoxide (NO) and nitrogen dioxide (NO_2)

default CESM/CAM simulation initialized from long-term CESM2.2 simulation. The atmospheric chemistry spin-up is run in a ne30 configuration, also for a year, but with full chemistry and including the aforementioned tags. For 2019, the ne30 simulation is simply continued for the complete period. For the ne30x4 simulation, the model initial conditions resulting from the ne30 simulation spin-up is regridded to the finer grid, and run together for a month with the output of the land spin-up, as a final spin-up step. The simulation is then continued for the entire year of 2019.

2.2 CO tagged tracers

We include a series of CO tagged tracers (hereafter CO tags) to identify transport of different sources. This approach has been previously used with various chemistry models (Gaubert et al., 2016; Tang et al., 2019; R. A. Fisher & Koven, 2020) to identify pollution origins and transport. The tags used in this study include 4 global CO tags according to the source type (anthropogenic, biomass burning, oceanic, biogenic). The sum of the four tags define the primary CO (Eq. 3).

$$\mathrm{CO_{primary}} = \mathrm{CO_{ant}} + \mathrm{CO_{bb}} + \mathrm{CO_{ocn}} + \mathrm{CO_{megan}} \tag{3}$$

We define the secondary CO by subtracting the primary CO from the modeled total CO (Eq. 4).

$$\mathrm{CO_{secondary}} = \mathrm{CO} - \mathrm{CO_{primary}} \tag{4}$$

We also define two tags to quantify the secondary CO resulting from the methane (CH_4) oxidation. CH_4 can be a major source of secondary CO, following complex reaction paths (Gaubert et al., 2016). Duncan et al. (2007) has reported a yield approaching unity using the model GEOS-Chem version 5.02, and a yield of 1 has been used in subsequent GEOS-Chem studies (J. A. Fisher et al., 2017). Gaubert et al. (2016) found a yield of 0.75 using CAM-Chem, due to the wet deposition of intermediate soluble species. To quantify the CH_4 source of secondary CO, two tags were added to Eq. 2 as shown in Eq. 5, one with a yield of 1 and another one assuming a yield of 0.75, without altering the other products of the oxidation of CH_4 by OH.

$$\mathrm{CH_4 + OH \rightarrow CH_3O_2 + H_2O + 0.75\,CO_{met0.75} + CO_{met1}} \tag{5}$$

Having an estimation of CO generated by methane allows us to estimate secondary CO generated by other VOCs, as shown in equation 6.

$$\mathrm{CO_{nmvoc}} = \mathrm{CO} - \mathrm{CO_{primary}} - \mathrm{CO_{met}} \tag{6}$$

We also define latitudinal tags for anthropogenic and biomass burning emissions, as described in table 1. Other geographical tags were defined as shown in Fig. 2. As in Gaubert et al. (2016), these tags are co-emitted and share the same dry deposition and chemical destruction rate as CO, but do not alter OH. We then estimate the contribution of each global source of CO (anthropogenic emissions, biomass burning emissions, emissions from the ocean, biogenic emissions and secondary CO). There is no specific tag for the secondary CO derived from NMVOCs, but it can be estimated as shown in Eq. 6 by choosing a yield for CH_4.

2.3 Model evaluation

The model is evaluated through comparison with gridded data from the Measurement Of Pollution In The Troposphere instrument (MOPITT) Level 3 data, on board of the Terra spacecraft. These retrievals have been used extensively to evaluate model

Tag	Geogr. Origin	Source
CO_{ant}	World	Anthropogenic emissions
CO_{bb}	World	Biomass burning emissions
CO_{ocn}	World	Ocean emissions
CO_{bio}	World	Biogenic emissions from land
$CO_{met0.75}$	World	Sec. Methane (yield=0.75)
CO_{met1}	World	Sec. Methane (yield=1)
CO_{bbSET}	lat: 90°S - 24°S	Biomass burning emissions
CO_{bbST}	lat: 24°S - 0°	Biomass burning emissions
CO_{bbNT}	lat: 0°N - 24°N	Biomass burning emissions
CO_{bbNET}	lat: 24°N - 90°N	Biomass burning emissions
CO_{antSET}	lat: 90°S - 24°S	Anthropogenic emissions
CO_{antST}	lat: 24°S - 0°S	Anthropogenic emissions
CO_{antNT}	lat: 0° - 24°N	Anthropogenic emissions
CO_{antNET}	lat: 24°N - 90°N	Anthropogenic emissions

Table 1. Global and latitudinal CO tags.

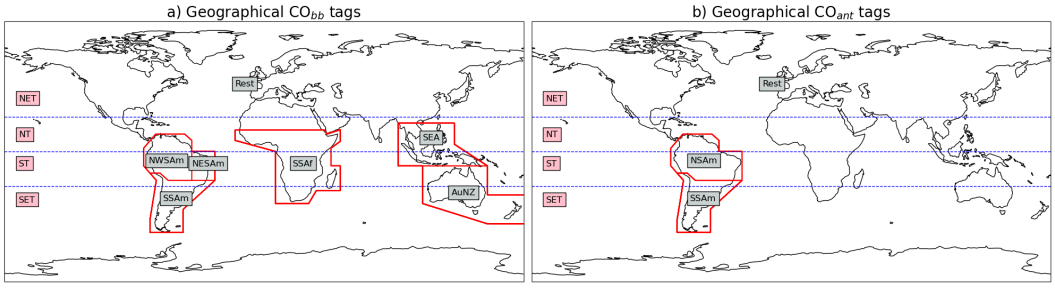

Figure 2. Geographical tags for biomass burning (bb) and anthropogenic (ant) CO (red). The latitudinal bands used for the latitudinal tags are also shown with a dashed blue line.

output (Daskalakis et al., 2022; Gaubert et al., 2020, 2016; Dekker et al., 2017). The output of the simulation is regridded to a 1° x 1° structured grid, and the MOPITT averaging kernel and *a priori* CO concentration are utilized as in Gaubert et al. (2016) to smooth dry-air column-averaged mole fraction (XCO) of the model in a way that can be compared to the satellite product. A simple subtraction in MOPITT space is applied for every simulated monthly mean.

The regionally refined model output is compared to the control (ne30) by regridding both outputs conservatively to a 0.25°-0.25° grid worldwide.

2.4 Evaluation of the main sources of CO and CO variability.

The mean tropospheric burden for each global tag is calculated for the complete simulation period. The standard deviation is also calculated utilizing the monthly means, to characterize the variability. The monthly means of the regional tags of figure 2 are used to evaluate the regional sources of CO as the year progresses.

The chemical lifetime of CO for each month is calculated as shown in equation 7.

$$\text{lifetime} = \text{CO}_{\text{burden}}/\text{CO}_{\text{CHML}}, \tag{7}$$

where CO_{CHML} is the integral of the CO chemical loss. Dry-air column averaged mole fractions of OH and isoprene are also used in the analysis to evaluate matching patterns.

Although most of South America (SAm) is in the Southern Hemisphere (SH), its northern tip stretches into the Northern Hemisphere (NH), including a portion of the Amazon rainforest. The latitudinal CO tags are used to evaluate cross-hemispheric transport, the effects that SAm might be having over each hemisphere and the effects of the NH over SAm.

The global relevance of SAm's primary emissions can be analyzed by adding the CO_{ant} and CO_{bb} tags from all the South American regions, and calculating the fraction of tagged CO over the total CO for any area of interest.

3 Results

3.1 Evaluation with MOPITT

In Fig. 3, we show the ne30x4 model bias compared to MOPITT XCO for four individual months during the year. The XCO comparison for all months can be found in the SI (Fig. S1). The analysis for the control run yielded similar results and is shown in Figure S2.

The general distribution of global CO is well represented in terms of the location of the hotspots. However, there are distinct biases in both hemispheres.

The simulated CO in the SH is generally higher than MOPITT retrievals. This applies to all of SAm, including the part of SAm that lies in the NH region. This is especially true during the biomass burning season, which starts in August and continues until the end of the year. In most months, the bias is below 20 ppbv, however, during the fire season, it can locally reach up to 90 ppbv. This high bias decreases rapidly further away from the fire hotspot, but it can remain at about 20–30 ppbv in the whole SH.

The version of FINN2.5 utilized provides the highest CO and VOC emissions of the commonly used fire emission inventories (Wiedinmyer et al., 2023). MOPITT and MODIS assimilation have shown important and large-scale positive biases in CO and aerosols (Gaubert et al., 2023). Some of the bias could be explained by the relative importance of the fire emissions in the SH combined with larger uncertainties in the anthropogenic emissions and the concentrations of other species (Paton-Walsh et al., 2022), including OH and bio-

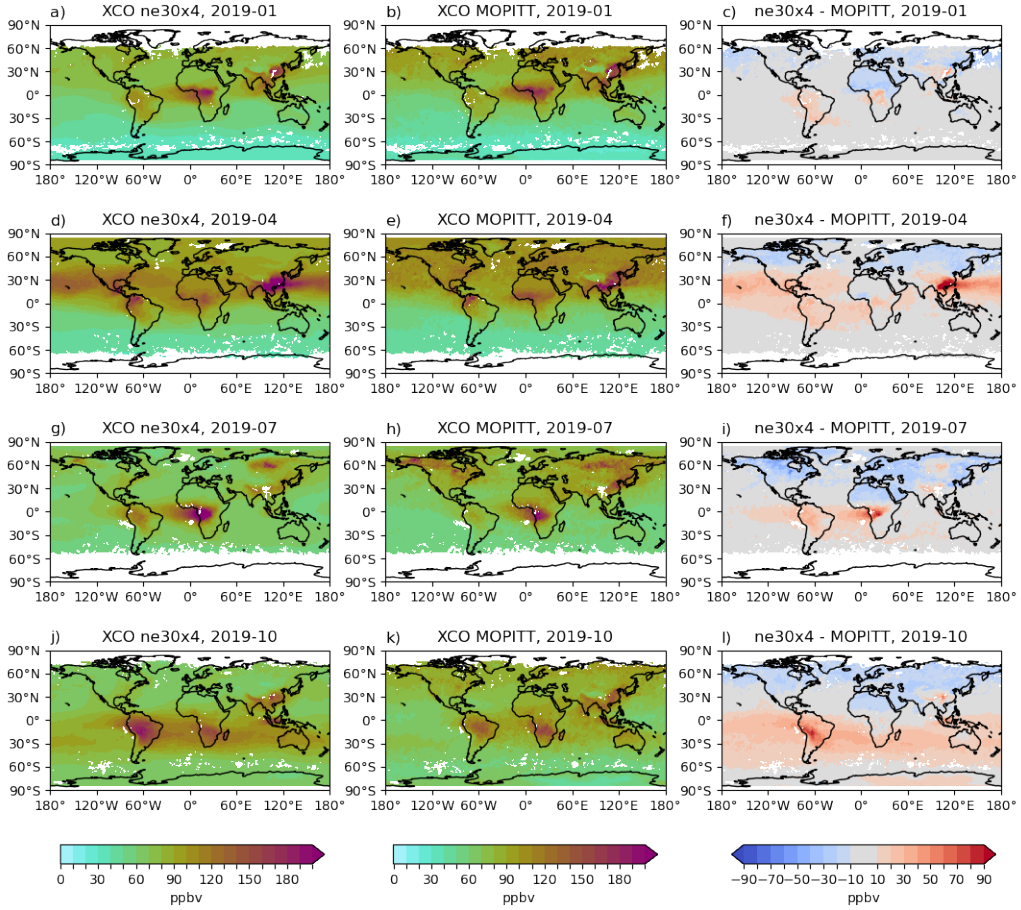

Figure 3. Model evaluation with MOPITT for the months of Jan, Apr, Jul, and Oct. See Fig. S1 for the total monthly difference for every simulated month. XCO represents the dry-air column averaged mole fraction. The model XCO is calculated by regridding to MOPITT space and using the MOPITT averaging kernel.

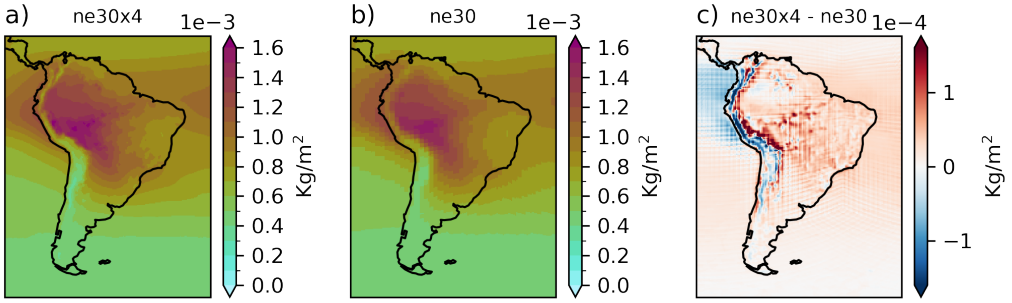

Figure 4. Annual mean CO burden over South America. a) ne30x4 refined simulation and b) ne30 control run. The absolute difference between the two is shown in c)

genic VOCs. It is unlikely that the fire inventory of choice is the only explanation, considering that Daskalakis et al. (2022), although studying a different time period, found similar bias patterns compared to MOPITT utilizing emissions from the Atmospheric Chemistry and Climate Intercomparison Project (ACCMIP) emission database and the offline chemical transport model TM4-ECPL.

3.2 CO budget

Here we compare the two different simulations (ne30 and ne30x4) in order to assess the impacts of a refined region over SAm. The higher resolution over the refined region is expected to better represent the sources and transport, thus also leading to changes in the chemistry and CO lifetimes. Table 2 shows the CO budget at the global scale and for South America.

SAm represents about 17% of the global CO emissions and 39% of the SH CO emissions. It includes 22% of the global biomass burning emissions, but only 9% of the global anthropogenic emissions. As shown in Table 2, the overall differences between the refined and the control grids in terms of the CO burden and budget estimates are fairly small.

There are, however, differences in the spatial distribution of the CO burden (Fig. 4). Part of these differences far from the refined region can be due to the ne30x4 grid being rotated with respect to the ne30 grid, which could have some global effects. Part of the differences, however, are likely also due to changes in the refined region, that could have global impacts either directly or indirectly due to meteorological feedbacks and transport. The mean dry-air column averaged OH mole fraction over the South-American continent is about the same in both simulations (0.64 ppt in ne30 vs 0.63 in ne30x4) but shows differences spatially (Fig. S4). When analyzing the different components of the budget, it is clear that the differences are mostly due to differences in chemical production and loss. The ne30x4 simulation has generally larger OH concentrations over the Andes, but smaller OH concentrations elsewhere. The CO burden in the ne30x4 simulation is smaller than the ne30 simulation to the west of the Andes, but larger to the east. Analyzing every tag, we find that the CO_{nmvoc} burden is actually smaller in the ne30x4 simulation on both sides of the Andes, likely due to less CO being produced from the oxidation of NMVOCs by OH. However, the CO_{bb} burden in the ne30x4 simulation is generally larger in the ne30 simulation over the continent. This is likely also the effect of less OH over the Amazon, and therefore less oxidation of CO_{bb}. When CO_{bb} travels over the Andes, however, it is oxidized. Therefore, CO west of the northern part of the continent is smaller in the ne30x4 simulation than in the control run.

Tag	Burden (Tg)	Net Budget (Tg/year)	Surf. Emis. (Tg/year)	Chem Prod (Tg/year)	Dry Dep (Tg/year)	Chem Loss (Tg/year)
			ne30, Global			
CO	343	-53	1400	1839	175	3117
CO_{ant}	62	-28	558	—	49	536
CO_{bb}	75	-18	734	—	68	683
CO_{ocn}	3	-1	22	—	0.6	22
CO_{bio}	9	-4	86	—	5	85
$CO_{met0.75}$	88	-3	—	811	21	794
CO_{nmvoc}	104	1	—	1028	31	996
			ne30x4, Global			
CO	349	-39	1399	1786	177	3047
CO_{ant}	64	-26	558	—	50	533
CO_{bb}	79	-11	734	—	69	676
CO_{ocn}	3	-1	20	—	0.6	20
CO_{bio}	9	-3	87	—	5	85
$CO_{met0.75}$	88	-3	—	782	21	765
CO_{nmvoc}	105	7	—	1005	30	967
			ne30, SAM			
CO	23	276	244	253	35	186
CO_{ant}	3	24	52	—	5	23
CO_{bb}	6	97	162	—	16	49
CO_{bio}	1	21	30	—	2	7
$CO_{met0.75}$	5	-3	—	40	4	39
CO_{nmvoc}	8	138	—	213	8	67
			ne30x4, SAM			
CO	23	279	244	242	35	172
CO_{ant}	3	24	51	—	5	22
CO_{bb}	7	101	162	—	16	45
CO_{bio}	1	22	30	—	2	7
$CO_{met0.75}$	5	-2	—	38	4	36
CO_{nmvoc}	8	136	—	204	8	61

Table 2. CO budget during 2019 for the global sources of CO in both simulations. In this table, a yield of 0.75 was assumed for Secondary CO derived from methane.

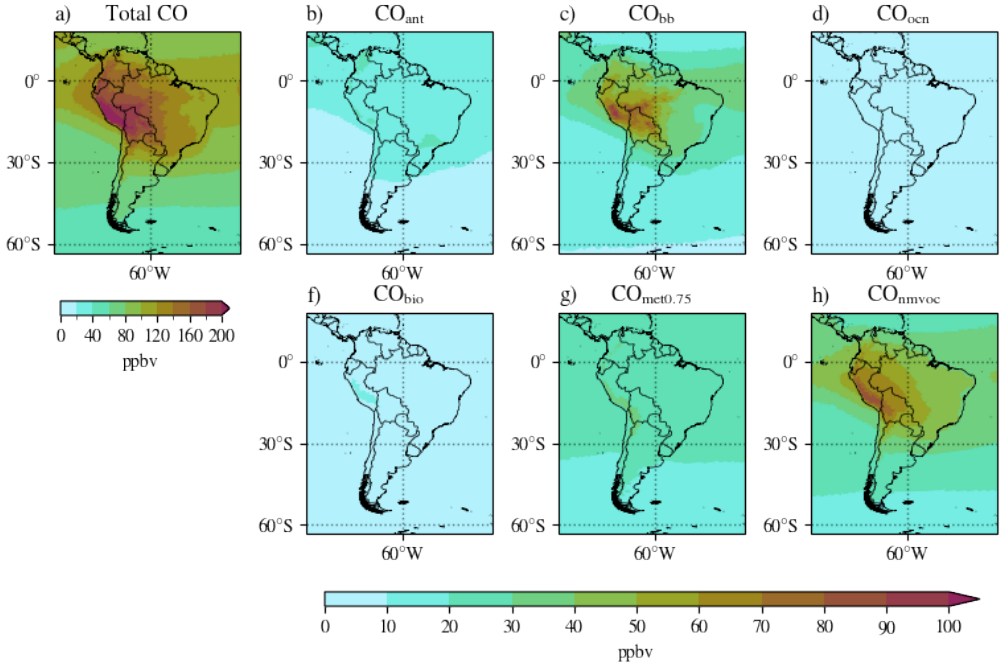

Figure 5. Annual mean CO tags. a) total CO, b) anthropogenic primary CO, c) biomass burning primary CO, d) ocean primary CO, f) biogenic primary CO, g) methane secondary CO assuming a yield of 0.75 and h) secondary CO from other (non-methane) sources. Note the different scales between the total CO in a) and the CO tags.

3.3 CO tag contribution

3.3.1 Global CO tags: annual analysis

In Fig. 5, we show the annual average concentration of CO and of each CO tag from the ne30x4 simulation. Most of the CO burden in the tropospheric column can be explained by either biomass burning emissions or secondary CO production. Biomass burning CO (Fig. 5b) is highest in the southern part of the Amazon Basin, and high concentrations are also shown in the westward plume transport to the Pacific Ocean.

The secondary CO (Fig. 5h) has maxima to the west of the Andes, over Peru and over northern Chile. This is, however, not necessarily a region with a high chemical production in the simulations. It also has relatively high OH concentrations, and the CO lifetime is, therefore, not particularly long (Fig. 6).

In Fig. 6, the mean CO chemical lifetime is shown together with the dry-air column averaged mole fraction of isoprene and OH. A longer chemical lifetime is simulated at higher latitudes because of a low OH under small solar radiation conditions. Conversely, the lifetime is shorter than 1 month in the tropics because of higher OH. The chemical lifetime of CO is relatively high in parts of the Amazon (160–180 days, compared to 30–90 days at similar latitudes outside the rainforest). As expected, the regions of long lifetime match regions of low OH. Jacob and Wofsy (1990) had already concluded that isoprene was the main OH sink over the Amazon rainforest, and Nölscher et al. (2016) reported a marked seasonality of OH reactivity modulated by biogenic emissions of NMVOCs. In the case of the rainforest, the region with long lifetimes matches almost perfectly re-

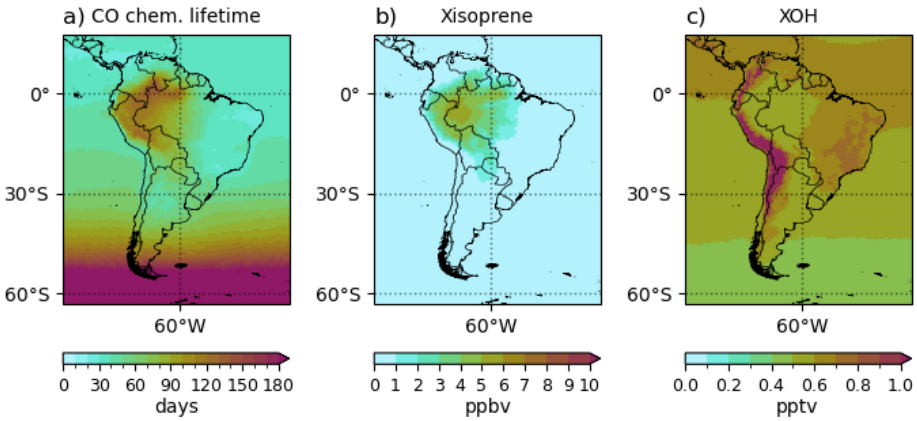

Figure 6. a) Annual mean CO lifetime (2019), b) dry-air column average mole fraction of isoprene and c) dry-air column average mole fraction of OH.

gions of high isoprene, which is probably destroying OH and reducing the chemical loss. Biogenic emissions and meteorology are affected by changing model resolution, and since isoprene is highly sensitive to temperature and reacts quickly with OH, this effect is assumed to account for some of the differences in chemical production and loss between the refined and control runs.

As shown in Fig. 7, while CO explains a large part of the burden all year round, CO_{bb} constitutes a smaller proportion until August, and increases significantly during the biomass burning season. The CO_{bb} burden has its peak in September, and slowly decreases over the following months. While having a smaller variation, CO_{nmvoc} also has values higher than the previous months during the biomass burning season. This is likely related to the emissions of other VOCs during biomass burning events, although other, less obvious effects might have an influence (including the effects that the biomass burning emissions might have over OH, total radiation, etc.).

The temporal variability of the CO monthly means (Fig 8) can be explained almost completely by biomass burning emissions. CH_4 in MUSICAv0 is prescribed in the lower vertical layers, which is the reason the standard deviation of $CO_{met0.75}$ is close to 0. Notice that there might still be minor variations due to the changes in OH concentrations, however.

A noticeable fact is that there are only minor variations in CO_{ant}, and these are mostly found in the region around São Paulo. Although the variability of CO_{bio} is close to zero, the effects of most of the biogenic emissions is probably in the changes in biogenic NMVOCs, and is therefore contained within the variability of CO_{nmvoc}. Although we believe that CO_{bb} is likely overestimated in the model, its dominant role in monthly variability remains true even if the total burden of CO_{bb} would be divided by three. It is therefore reasonable to focus mostly on CO_{bb} to understand the changes and sources of CO variability over the course the year.

3.3.2 Temporal and geographical analysis of biomass burning primary CO

In the right column of Fig. 7 the burden of the different CO_{bb} tags are shown for selected regions. For all of SAM, CO_{bb} ranges from 16% of the total CO in January to

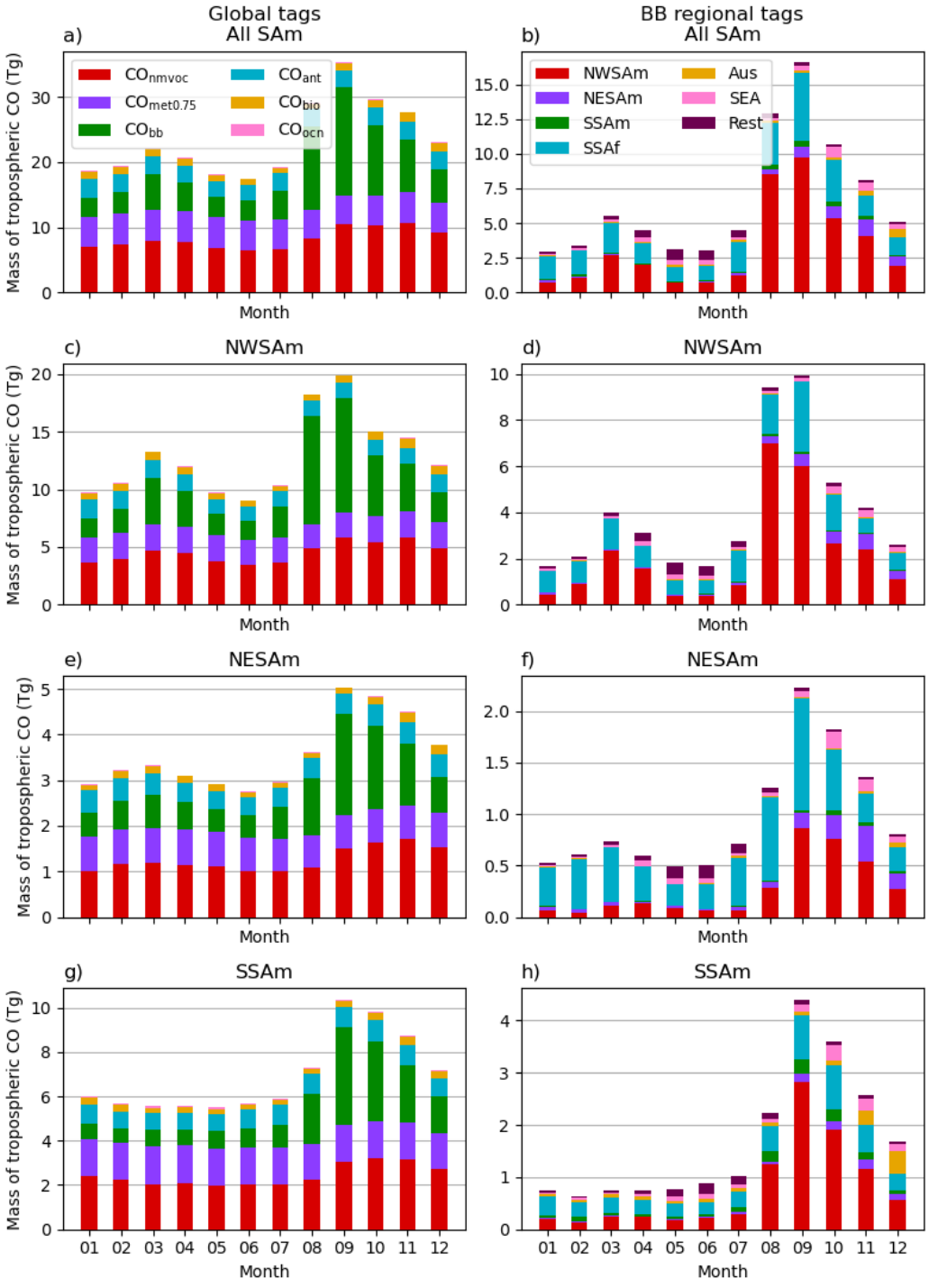

Figure 7. Stacked bar plot of the burden of CO for each tag. The left column represents global tags by CO source, whereas the right column represents the geographical tags for CO_{bb}. The regions are defined as shown in Fig. 2a). Note that each region has different areas and, therefore, the total burden should not be compared directly with each other. The sum of NWSAm, NESAm and SSAm does, however, equal All SAm.

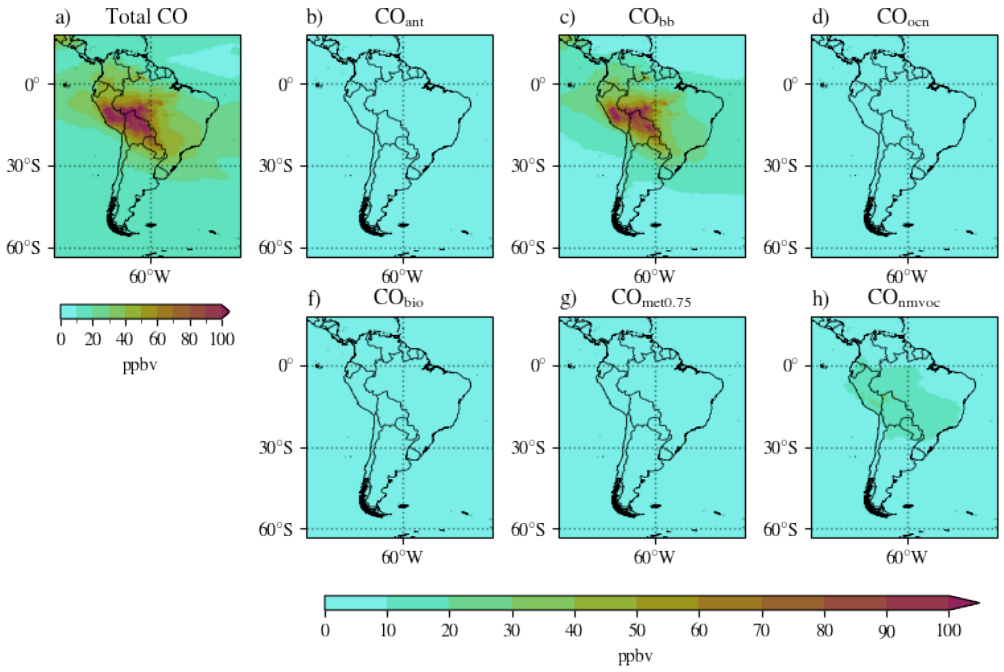

Figure 8. Standard deviation of the monthly means for each global tag. a) is the total CO, b) is anthropogenic primary CO, c) is the biogenic primary CO, d) is the ocean primary CO, f) is the biogenic primary CO, g) is the secondary CO derived from methane with a yield of 0.75 and h) is the non-methane derived secondary CO.

47% of the total CO in September. Looking at the individual CO_{bb} tags (see Fig. 2a), it is clear that a large portion of the CO_{bb} is from Africa all year round. As a percentage of the total CO burden in all of SAM, it ranges from 5% in November to 14% of the total CO in September. This applies even to SSAm, which is furthest away from Africa. In SSAm, it is 4%-9% of the total CO burden. As a percentage of the total primary biomass burning CO burden, it is 19%–48%, and is the largest contributor up to the Amazon fires in August.

The biomass burning pattern over the Amazon (i.e., NWSAm) is clearly visible. The contribution of $CO_{bbNWSAm}$ to the total SAm burden during September is ∼10 times larger than during May. It is worth noting that the peak of $CO_{bbNWSAm}$ in all of SAm during September does not match the peak of $CO_{bbNWSAm}$ in the region of NWSAm during August. This is a clear sign of the long lifetime of CO, and slower fluxes in the region, with the compound effects of CO slowly accumulating over the continent over multiple months, causing a 1-month delay in the peak. During 2019, there is also a compound effect of the SSAf and Amazonian fires, which have their maximum contribution to the burden during August and September. 2019 was a year of few biomass burning events in SSAm, which is reflected in its low contribution to the CO_{bb} burden.

Africa has two clearly distinct fire seasons, north and south of the equator. Transport from African biomass burning into the Amazon has been reported in previous studies, and its effects in the aerosol cycling have been extensively researched (Barkley et al., 2019; Holanda et al., 2023). We quantify the impact of African biomass burning emissions for CO, and find that the African contribution to the total CO burden in NWSAm ranges from 4% in November to 15% in September. The magnitude of the effect in September is especially relevant, taking into account that it is the month with the overall largest CO burden in that region. NESAm is the entry point of fluxes from Central Africa into South America. This remains true during both African biomass burning seasons (north and south of the equator). In NESAm, the CO_{bbSSAf} burden is 79% of the total CO_{bb} in February, although this only accounts to 15% of the total CO burden in the region. In November, the month with the lowest percentage contribution, it is only about 6% of the total CO burden, but remains at 20% of the CO_{bb}.

In SSAm, while biomass burning from NWSAm and SSAf are estimated to be predominant during most of the year, the effects of the Australian fires becomes apparent during the peak biomass burning in December 2019.

3.3.3 South America's effect on the rest of the world

In Fig. 9 we demonstrate the effects of the South American CO primary emissions on the rest of the world. During the biomass burning season, SAm primary emissions can increase the CO concentration considerably in the entire Southern Hemisphere, with a large effect over the southern tip of Africa (up to 50 ppbv in the column averaged mole fraction in our simulation, which accounts for about 30% of the total CO concentration). Following wind patterns, CO travels towards the Pacific Ocean in the northeast, and towards the west over the Atlantic at about 15°S–30°S of the continent. The results also show effects over SEA and Australia, reaching up to 30 ppbv during October (∼25% of the total CO concentration over these regions).

The effects over the Northern Hemisphere are overall minor and are limited to the oceans or close to the equator because of the much higher CO contributions from NH sources. Fig. 9 shows a relatively strong flux of CO from the northern Amazon into the tropical Pacific Ocean.

The CO that is transported to the tropical Pacific gets well mixed zonally, and some of it might reenter the continent from the east.

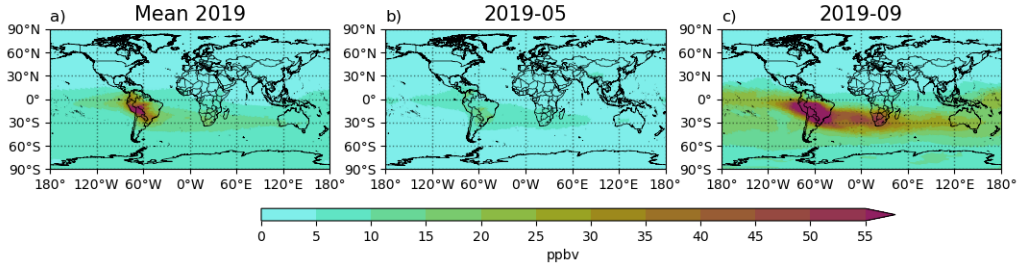

Figure 9. Summary of the effect of South American primary emissions over the rest of the world. In subplot a), the yearly mean is shown. In subplot b), we show the monthly mean for May, a month with low BB emissions, and in subplot c), September is chosen as an example of a month with large biomass burning over the Amazon.

4 Conclusions

The main conclusions from this paper can be summarized as follows:

1. We present the first application and evaluation of MUSICAv0 to the entire South American continent. Our refined grid (ne30x4) includes a global 1°x1° model with a refinement up to 28 km over South America. We present the results for the year 2019 and evaluate the impact of the refined grid. The simulated trace gases and dynamics are comparable to the standard configuration of CAM-Chem with a spectral element dynamical core and standard grid configuration (ne30).
2. We quantify the CO budget for the year 2019, and characterize the contribution from different emission/chemical sources and geographical origin using CO tags. The biomass burning emissions play an overwhelming role in the continental budget, and are the main factor of temporal variability. They also explain the majority of the temporal variability in CO columns. However, our comparison with MOPITT suggests that FINN2.5 is overestimating biomass burning emissions in the Southern Hemisphere.
3. The effects of the model spatial resolution leads to minor changes in the CO budget, driven by changes in the chemical production and loss. Higher resolution implies more localized biogenic emissions of multiple species (including isoprene), which in turn affects OH. There are also minor variations in the temperature, which can have a large effect on isoprene emissions. Changes in temperature and other meteorological parameters will also affect atmospheric chemistry per se.
4. Biomass burning activities in Africa are a relevant source of CO in all of SAm, including the South. This is the case during for all seasons, in the early months of 2019 we find a cross-equatorial flux of African biomass sources. Outside of the Amazon biomass burning season, they represent the largest source of CO_{bb}.
5. CO is estimated to have a long chemical lifetime over the Amazon in our simulations, determined by low OH concentrations. This is likely due to large isoprene emissions. The biogenic emissions over the Amazon play two different roles in the CO budget. As VOC emitters, they are a relevant source of secondary CO. At the same time, they destroy OH, leading to a longer chemical lifetime, but lower chemical production and loss. Further study is needed to understand the exact net effect, and would require a more complex tagged CO production from biogenic NMVOCs to be included in the model.
6. SAm's primary emissions are relevant contributors to CO in the SH, but show only minor influence on the NH. The largest effects in the SH are over the southern tip

of Africa, with smaller but relevant effects over the Maritime Continent, New Zealand, Australia and South East Asia.

Future perspectives

Understanding the CO budget and chemistry in South America is far from a well characterized problem yet is essential to understanding air quality and human and environmental impacts. For modeling studies, there is a need to further tackle the emission inventories, understand sources of model biases and correct for them. Some useful and important work has been done in regard to improving anthropogenic inventories (Ibarra-Espinosa et al., 2018; Castesana et al., 2022; Álamos et al., 2022), but there is no regionally concerted effort to maintain a high quality anthropogenic emission inventory for the whole region which is regularly updated. As shown in this paper, at the same time tackling uncertainties in biomass burning sources is of very high importance.

Measurement campaigns have been performed in different parts of the continent, but there are few operational urban air quality stations and even fewer over remote sites. These sites are located mostly in the Amazon, parts of Chile, and Colombia. There are also relevant observatories, like the Amazon Tall Tower Observatory, the Chacaltaya and the Ushuaia GAW stations. However, coverage is rather sparse and there are many regions without relevant observations. In addition, data access and availability is a major obstacle, e.g., Argentina lacks a centralized database to access available data.

With the formation of the Latin America Early Career Earth System Scientist Network (Yáñez-Serrano et al., 2022) and the Southern Hemisphere Working Group of the International Global Atmospheric Chemistry (IGAC) project (Paton-Walsh et al., 2022), a stronger scientific community is starting to focus on the region.

Further studies and observations are needed, especially in the southern part of the continent (i.e., SSAm). There, there is also a large amount of small fires that might not be captured by the satellites, and large territories with no observation sites, which could provide useful information on CO chemistry and air quality in general.

Open Research

CESM2.2 (including MUSICAv0) is a publicly released version of the Community Earth System Model that is available at `https://www.cesm.ucar.edu/` (last access: 15 March 2023). The MERRA-2 data and FINN2.5 are available at the National Center for Atmospheric Research's Research Data Archive (Atmospheric Chemistry Observations & Modeling, National Center for Atmospheric Research, University Corporation for Atmospheric Research & Climate and Global Dynamics Division, National Center for Atmospheric Research, University Corporation for Atmospheric Research, 2018). The CAMS-GLOB-ANT v5.3 and CAMS-GLOB-AIR v2.1 anthropogenic emissions are available at `https://eccad.sedoo.fr/#/catalogue` (last access: 15 March 2023). The MOPITT gridded monthly means are available at `https://search.earthdata.nasa.gov/` (last access: 3 September 2023).

Acknowledgments

This material is based upon work supported by the National Center for Atmospheric Research, which is a major facility sponsored by the National Science Foundation under Cooperative Agreement No. 1852977. Computing resources were provided by NSF NCAR's Computational and Information Systems Laboratory (CISL). This work also used resources of the Deutsches Klimarechenzentrum (DKRZ) granted by its Scientific Steering Committee (WLA) under project IDs bm1234 and mh0735. The authors would

also like to acknowledge the EU Horizon 2020 Marie Skłodowska-Curie project PAPILA (grant no. 777544; MSCA action for research and innovation staff exchange).

References

Álamos, N., Huneeus, N., Opazo, M., Osses, M., Puja, S., Pantoja, N., ... Calvo, R. (2022). High-resolution inventory of atmospheric emissions from transport, industrial, energy, mining and residential activities in Chile. *Earth System Science Data*, *14*(1), 361–379. doi: 10.5194/essd-14-361-2022

Atmospheric Chemistry Observations & Modeling, National Center for Atmospheric Research, University Corporation for Atmospheric Research, & Climate and Global Dynamics Division, National Center for Atmospheric Research, University Corporation for Atmospheric Research. (2018). *Merra2 global atmosphere forcing data.* Boulder CO: Research Data Archive at the National Center for Atmospheric Research, Computational and Information Systems Laboratory. Retrieved from `https://doi.org/10.5065/XVAQ-2X07`

Barkley, A. E., Prospero, J. M., Mahowald, N., Hamilton, D. S., Popendorf, K. J., Oehlert, A. M., ... Gaston, C. J. (2019). African biomass burning is a substantial source of phosphorus deposition to the Amazon, Tropical Atlantic Ocean, and Southern Ocean. *Proceedings of the National Academy of Sciences*, *116*(33), 16216–16221. doi: 10.1073/pnas.1906091116

Bogenschutz, P. A., Gettelman, A., Morrison, H., Larson, V. E., Craig, C., & Schanen, D. P. (2013). Higher-Order Turbulence Closure and Its Impact on Climate Simulations in the Community Atmosphere Model. *Journal of Climate*, *26*(23), 9655–9676. doi: 10.1175/jcli-d-13-00075.1

Castesana, P., Resquin, M. D., Huneeus, N., Puliafito, E., Darras, S., Gómez, D., ... Dawidowski, L. (2022). PAPILA dataset: a regional emission inventory of reactive gases for South America based on the combination of local and global information. *Earth System Science Data*, *14*(1), 271–293. doi: 10.5194/essd-14-271-2022

Danabasoglu, G., Lamarque, J.-F., Bacmeister, J., Bailey, D. A., DuVivier, A. K., Edwards, J., ... Strand, W. G. (2020). The Community Earth System Model Version 2 (CESM2). *Journal of Advances in Modeling Earth Systems*, *12*(2). doi: 10.1029/2019ms001916

Daskalakis, N., Gallardo, L., Kanakidou, M., Nüß, J. R., Menares, C., Rondanelli, R., ... Vrekoussis, M. (2022). Impact of biomass burning and stratospheric intrusions in the remote South Pacific Ocean troposphere. *Atmospheric Chemistry and Physics*, *22*(6), 4075–4099. doi: 10.5194/acp-22-4075-2022

Dekker, I. N., Houweling, S., Aben, I., Röckmann, T., Krol, M., Martínez-Alonso, S., ... Worden, H. M. (2017). Quantification of CO emissions from the city of Madrid using MOPITT satellite retrievals and WRF simulations. *Atmospheric Chemistry and Physics*, *17*(23), 14675–14694. doi: 10.5194/acp-17-14675-2017

de Miranda, P. L. S., Dexter, K. G., Swaine, M. D., de Oliveira-Filho, A. T., Hardy, O. J., & Fayolle, A. (2022). Dissecting the difference in tree species richness between Africa and South America. *Proceedings of the National Academy of Sciences*, *119*(14). doi: 10.1073/pnas.2112336119

Duncan, B. N., Logan, J. A., Bey, I., Megretskaia, I. A., Yantosca, R. M., Novelli, P. C., ... Rinsland, C. P. (2007). Global budget of CO, 1988-1997: Source estimates and validation with a global model. *Journal of Geophysical Research*, *112*(D22). doi: 10.1029/2007jd008459

Edwards, D. P. (2004). Observations of carbon monoxide and aerosols from the terra satellite: Northern hemisphere variability. *Journal of Geophysical Research*, *109*(D24). doi: 10.1029/2004jd004727

Emmons, L. K., Schwantes, R. H., Orlando, J. J., Tyndall, G., Kinnison, D., Lamar-

que, J.-F., ... Pétron, G. (2020). The Chemistry Mechanism in the Community Earth System Model Version 2 (CESM2). *Journal of Advances in Modeling Earth Systems*, *12*(4). doi: 10.1029/2019ms001882

Fisher, J. A., Murray, L. T., Jones, D. B. A., & Deutscher, N. M. (2017). Improved method for linear carbon monoxide simulation and source attribution in atmospheric chemistry models illustrated using GEOS-Chem v9. *Geoscientific Model Development*, *10*(11), 4129–4144. doi: 10.5194/gmd-10-4129-2017

Fisher, R. A., & Koven, C. D. (2020). Perspectives on the Future of Land Surface Models and the Challenges of Representing Complex Terrestrial Systems. *Journal of Advances in Modeling Earth Systems*, *12*(4). doi: 10.1029/2018ms001453

Gaubert, B., Arellano, A. F., Barré, J., Worden, H. M., Emmons, L. K., Tilmes, S., ... Jones, N. (2016). Toward a chemical reanalysis in a coupled chemistry-climate model: An evaluation of MOPITT CO assimilation and its impact on tropospheric composition. *Journal of Geophysical Research: Atmospheres*, *121*(12), 7310–7343. doi: 10.1002/2016jd024863

Gaubert, B., Edwards, D. P., Anderson, J. L., Arellano, A. F., Barré, J., Buchholz, R. R., ... Ziskin, D. (2023). Global Scale Inversions from MOPITT CO and MODIS AOD. *Remote Sensing*, *15*(19), 4813. doi: 10.3390/rs15194813

Gaubert, B., Emmons, L. K., Raeder, K., Tilmes, S., Miyazaki, K., Jr., A. F. A., ... Diskin, G. S. (2020). Correcting model biases of CO in East Asia: impact on oxidant distributions during KORUS-AQ. *Atmospheric Chemistry and Physics*, *20*(23), 14617–14647. doi: 10.5194/acp-20-14617-2020

Gaubert, B., Worden, H. M., Arellano, A. F. J., Emmons, L. K., Tilmes, S., Barré, J., ... Edwards, D. P. (2017). Chemical Feedback From Decreasing Carbon Monoxide Emissions. *Geophysical Research Letters*, *44*(19), 9985–9995. doi: 10.1002/2017gl074987

Gelaro, R., McCarty, W., Suárez, M. J., Todling, R., Molod, A., Takacs, L., ... Zhao, B. (2017). The Modern-Era Retrospective Analysis for Research and Applications, Version 2 (MERRA-2). *Journal of Climate*, *30*(14), 5419–5454. doi: 10.1175/jcli-d-16-0758.1

Gettelman, A., & Morrison, H. (2015). Advanced Two-Moment Bulk Microphysics for Global Models. Part i: Off-Line Tests and Comparison with Other Schemes. *Journal of Climate*, *28*(3), 1268–1287. doi: 10.1175/jcli-d-14-00102.1

Grant, A., Archibald, A. T., Cooke, M. C., & Shallcross, D. E. (2010). Modelling the oxidation of seventeen volatile organic compounds to track yields of CO and CO2. *Atmospheric Environment*, *44*(31), 3797–3804. doi: 10.1016/j.atmosenv.2010.06.049

Guenther, A. B., Jiang, X., Heald, C. L., Sakulyanontvittaya, T., Duhl, T., Emmons, L. K., & Wang, X. (2012). The Model of Emissions of Gases and Aerosols from Nature version 2.1 (MEGAN2.1): an extended and updated framework for modeling biogenic emissions. *Geoscientific Model Development*, *5*(6), 1471–1492. doi: 10.5194/gmd-5-1471-2012

Holanda, B. A., Franco, M. A., Walter, D., Artaxo, P., Carbone, S., Cheng, Y., ... Pöhlker, C. (2023). African biomass burning affects aerosol cycling over the amazon. *Communications Earth &amp Environment*, *4*(1). doi: 10.1038/s43247-023-00795-5

Ibarra-Espinosa, S., Ynoue, R., O'Sullivan, S., Pebesma, E., de Fátima Andrade, M., & Osses, M. (2018). VEIN v0.2.2: an R package for bottom–up vehicular emissions inventories. *Geoscientific Model Development*, *11*(6), 2209–2229. doi: 10.5194/gmd-11-2209-2018

Jacob, D. J., & Wofsy, S. C. (1990). Budgets of reactive nitrogen, hydrocarbons, and ozone over the amazon forest during the wet season. *Journal of Geophysical Research: Atmospheres*, *95*(D10), 16737–16754. doi:

10.1029/jd095id10p16737

Jo, D. S., Emmons, L. K., Callaghan, P., Tilmes, S., Woo, J.-H., Kim, Y., ... Kanaya, Y. (2023). Comparison of Urban Air Quality Simulations During the KORUS-AQ Campaign With Regionally Refined Versus Global Uniform Grids in the Multi-Scale Infrastructure for Chemistry and Aerosols (MUSICA) Version 0. *Journal of Advances in Modeling Earth Systems*, *15*(7). doi: 10.1029/2022ms003458

Jo, D. S., Hodzic, A., Emmons, L. K., Tilmes, S., Schwantes, R. H., Mills, M. J., ... Jimenez, J. L. (2021). Future changes in isoprene-epoxydiol-derived secondary organic aerosol (IEPOX SOA) under the Shared Socioeconomic Pathways: the importance of physicochemical dependency. *Atmospheric Chemistry and Physics*, *21*(5), 3395–3425. doi: 10.5194/acp-21-3395-2021

Lauritzen, P. H., Nair, R. D., Herrington, A. R., Callaghan, P., Goldhaber, S., Dennis, J. M., ... Tribbia, J. J. (2018). NCAR release of CAM-SE in CESM2.0: A Reformulation of the Spectral Element Dynamical Core in Dry-Mass Vertical Coordinates With Comprehensive Treatment of Condensates and Energy. *Journal of Advances in Modeling Earth Systems*, *10*(7), 1537–1570. doi: 10.1029/2017ms001257

Lawrence, D. M., Fisher, R. A., Koven, C. D., Oleson, K. W., Swenson, S. C., Bonan, G., ... Zeng, X. (2019). The Community Land Model Version 5: Description of New Features, Benchmarking, and Impact of Forcing Uncertainty. *Journal of Advances in Modeling Earth Systems*, *11*(12), 4245–4287. doi: 10.1029/2018ms001583

Levy, H. (1971). Normal Atmosphere: Large Radical and Formaldehyde Concentrations Predicted. *Science*, *173*(3992), 141–143. doi: 10.1126/science.173.3992.141

Liu, X., Ma, P.-L., Wang, H., Tilmes, S., Singh, B., Easter, R. C., ... Rasch, P. J. (2016). Description and evaluation of a new four-mode version of the Modal Aerosol Module (MAM4) within version 5.3 of the Community Atmosphere Model. *Geoscientific Model Development*, *9*(2), 505–522. doi: 10.5194/gmd-9-505-2016

Müller, J.-F., Stavrakou, T., Bauwens, M., George, M., Hurtmans, D., Coheur, P.-F., ... Sweeney, C. (2018). Top-Down CO Emissions Based On IASI Observations and Hemispheric Constraints on OH Levels. *Geophysical Research Letters*, *45*(3), 1621–1629. doi: 10.1002/2017gl076697

Naik, V., Voulgarakis, A., Fiore, A. M., Horowitz, L. W., Lamarque, J.-F., Lin, M., ... Zeng, G. (2013). Preindustrial to present-day changes in tropospheric hydroxyl radical and methane lifetime from the Atmospheric Chemistry and Climate Model Intercomparison P10.1029/2019gl085706roject (ACCMIP). *Atmospheric Chemistry and Physics*, *13*(10), 5277–5298. doi: 10.5194/acp-13-5277-2013

Novelli, P. C. (2003). Reanalysis of tropospheric CO trends: Effects of the 1997–1998 wildfires. *Journal of Geophysical Research*, *108*(D15). doi: 10.1029/2002jd003031

Nölscher, A. C., Yañez-Serrano, A. M., Wolff, S., de Araujo, A. C., Lavrič, J. V., Kesselmeier, J., & Williams, J. (2016). Unexpected seasonality in quantity and composition of amazon rainforest air reactivity. *Nature Communications*, *7*(1). doi: 10.1038/ncomms10383

Paton-Walsh, C., Emmerson, K. M., Garland, R. M., Keywood, M., Hoelzemann, J. J., Huneeus, N., ... Olivares, G. (2022). Key challenges for tropospheric chemistry in the Southern Hemisphere. *Elementa: Science of the Anthropocene*, *10*(1). doi: 10.1525/elementa.2021.00050

Pfister, G. G., Eastham, S. D., Arellano, A. F., Aumont, B., Barsanti, K. C., Barth, M. C., ... Brasseur, G. P. (2020). The Multi-Scale Infrastructure for Chemistry and Aerosols (MUSICA). *Bulletin of the American Meteorological Soci-*

ety, *101*(10), E1743–E1760. doi: 10.1175/bams-d-19-0331.1

Pfister, G. G., Emmons, L. K., Hess, P. G., Lamarque, J.-F., Orlando, J. J., Walters, S., ... Lawrence, P. J. (2008). Contribution of isoprene to chemical budgets: A model tracer study with the NCAR CTM MOZART-4. *Journal of Geophysical Research: Atmospheres*, *113*(D5), n/a–n/a. doi: 10.1029/2007jd008948

Schwantes, R. H., Lacey, F. G., Tilmes, S., Emmons, L. K., Lauritzen, P. H., Walters, S., ... Wisthaler, A. (2022). Evaluating the Impact of Chemical Complexity and Horizontal Resolution on Tropospheric Ozone Over the Conterminous US With a Global Variable Resolution Chemistry Model. *Journal of Advances in Modeling Earth Systems*, *14*(6). doi: 10.1029/2021ms002889

Seinfeld, J. H., & Pandis, S. N. (2016). *Atmospheric chemistry and physics: from air pollution to climate change*. John Wiley & Sons.

Shindell, D. T., Faluvegi, G., Stevenson, D. S., Krol, M. C., Emmons, L. K., Lamarque, J.-F., ... Zeng, G. (2006). Multimodel simulations of carbon monoxide: Comparison with observations and projected near-future changes. *Journal of Geophysical Research*, *111*(D19). doi: 10.1029/2006jd007100

Soulie, A., Granier, C., Darras, S., Zilbermann, N., Doumbia, T., Guevara, M., ... Smith, S. (2023). Global Anthropogenic Emissions (CAMS-GLOB-ANT) for the Copernicus Atmosphere Monitoring Service Simulations of Air Quality Forecasts and Reanalyses. *Earth Syst. Sci. Data Discuss.*. doi: 10.5194/essd-2023-306

Stein, O., Schultz, M. G., Bouarar, I., Clark, H., Huijnen, V., Gaudel, A., ... Clerbaux, C. (2014). On the wintertime low bias of Northern Hemisphere carbon monoxide found in global model simulations. *Atmospheric Chemistry and Physics*, *14*(17), 9295–9316. doi: 10.5194/acp-14-9295-2014

Stone, D., Whalley, L. K., & Heard, D. E. (2012). Tropospheric OH and HO2 radicals: field measurements and model comparisons. *Chemical Society Reviews*, *41*(19), 6348. doi: 10.1039/c2cs35140d

Tang, W., Emmons, L. K., Buchholz, R. R., Wiedinmyer, C., Schwantes, R. H., He, C., ... Campos, T. L. (2022). Effects of fire diurnal variation and plume rise on U.S. air quality during FIREX-AQ and WE-CAN based on the Multi-Scale Infrastructure for Chemistry and Aerosols (MUSICAv0). *Journal of Geophysical Research: Atmospheres*. doi: 10.1029/2022jd036650

Tang, W., Emmons, L. K., Jr, A. F. A., Gaubert, B., Knote, C., Tilmes, S., ... Kim, D. (2019). Source contributions to carbon monoxide concentrations during KORUS-AQ based on CAM-chem model applications. *Journal of Geophysical Research: Atmospheres*, *124*(5), 2796–2822. doi: 10.1029/2018jd029151

Tang, W., Emmons, L. K., Worden, H. M., Kumar, R., He, C., Gaubert, B., ... Levelt, P. (2023). Application of the multi-scale infrastructure for chemistry and aerosols version 0 (MUSICAv0) for air quality research in africa. *Geoscientific Model Development*, *16*(20), 6001–6028. doi: 10.5194/gmd-16-6001-2023

Tilmes, S., Hodzic, A., Emmons, L. K., Mills, M. J., Gettelman, A., Kinnison, D. E., ... Liu, X. (2019). Climate Forcing and Trends of Organic Aerosols in the Community Earth System Model (CESM2). *Journal of Advances in Modeling Earth Systems*, *11*(12), 4323–4351. doi: 10.1029/2019ms001827

Watson, C. E., Fishman, J., & Reichle, H. G. (1990). The significance of biomass burning as a source of carbon monoxide and ozone in the southern hemisphere tropics: A satellite analysis. *Journal of Geophysical Research: Atmospheres*, *95*(D10), 16443–16450. doi: 10.1029/jd095id10p16443

Wiedinmyer, C., Kimura, Y., McDonald-Buller, E. C., Emmons, L. K., Buchholz, R. R., Tang, W., ... Yokelson, R. (2023). The Fire Inventory from NCAR version 2.5: an updated global fire emissions model for climate and chemistry applications. *Geoscientific Model Development*, *16*(13), 3873–3891. doi:

10.5194/gmd-16-3873-2023

Yáñez-Serrano, A. M., Aguilos, M., Barbosa, C., Bolaño-Ortiz, T. R., Carbone, S., Díaz-López, S., ... Tzompa-Sosa, Z. A. (2022). The latin america early career earth system scientist network (LAECESS): addressing present and future challenges of the upcoming generations of scientists in the region. *npj Climate and Atmospheric Science*, *5*(1). doi: 10.1038/s41612-022-00300-3

Zhang, G., & McFarlane, N. A. (1995). Sensitivity of climate simulations to the parameterization of cumulus convection in the Canadian climate centre general circulation model. *Atmosphere-Ocean*, *33*(3), 407–446. doi: 10.1080/07055900.1995.9649539